Check for updates

Hexadecylamine functionalised graphene quantum dots as suitable nano-adsorbents for phenanthrene removal from aqueous solution

Gugu Kubheka, Adedapo O. Adeola and Patricia B. C. Forbes ⓘD *

In this study, three novel hexadecylamine graphene quantum dots (hexadecyl-GQDs) with varying moieties on the surface were synthesised and characterised to examine the effect of surface functionalisation on their adsorption efficiency. Introducing hydrophobic moieties *via in situ* generation of an amide bond by coupling hydrophilic carboxylic acid-functionalised GQDs with hexadecylamine improved the adsorption capacity of GQDs. The AFM and Raman spectroscopy results revealed the formation of multilayered GQDs with an average diameter of 10.0, 9.8, and 7.0 nm for C_{16}-GQDs, C_{16}-NGQDs and C_{16}-SNGQDs, respectively. According to the sum of squared error (SSE) values obtained from fitting phenanthrene adsorption experimental data to two- and three-parameter models, the Sips hybrid isotherm model best described the adsorption of sorbate to the doped hexadecyl-GQDs ($0.55 \geq SSE \leq 0.72$), with R^2 values >0.9. Furthermore, doping of the GQDs favoured a multilayer adsorption mechanism over monolayer adsorption, enhancing adsorption capacities (K_F & K_d). Hexadecylamine sulphur and nitrogen co-doped GQDs (C_{16}-SNGQDs) gave the highest maximum adsorption capacity (q_m) of ~1377 mg g^{-1}. Pristine GQDs interact with phenanthrene endothermically, while the adsorption of phenanthrene onto modified GQDs is spontaneously exothermic. The adsorption of phenanthrene is most affected by the presence of sulfate and phosphate anions and is best at ambient temperature and acidic pH. Co-doping with nitrogen and sulphur groups and modification of hydrophilic to hydrophobic form enhanced the physicochemical and adsorption performance of C_{16}-SNGQDs, making them potentially suitable as materials for the extraction of hydrophobic organic pollutants from water.

Introduction

The increase in industrial and agricultural activities poses a risk of introducing harmful pollutants into the environment, and this has motivated substantial research effort, especially in developing materials and improving existing techniques for removing environmental contaminants.[1] Although numerous toxic organic and inorganic species are potentially generated at such sites, polycyclic aromatic hydrocarbons (PAHs) are one of the most ubiquitous classes of organic contaminants produced by anthropogenic activities as a result of industrialisation and urbanisation.[2–4] PAHs are comprised of two or more benzene rings bonded in differently shaped arrangements.[5] Furthermore, 16 PAHs have been categorised as priority contaminants based on possible human exposure, level of toxicity, and the extent of information available.[6] Amongst these PAHs is phenanthrene due to its potential mutagenicity, carcinogenicity, toxicity, and bioaccumulation.[7] Phenanthrene is a low molecular weight PAH which is characterised by three fused benzene

rings with enhanced hydrophobicity and low biodegradability due to its chemical stability.[8,9] In addition, PAHs pose risks to aquatic organisms like fish because of their propensity to bioaccumulate, which subsequently constitutes a potential human exposure route through the dietary pathway.[10,11] Therefore, attention to PAH polluted water is warranted, and effective measures to purify it to reduce negative environmental impacts are most important.[12,13] Furthermore, the presence of dissolved and suspended solids and natural organic matter in the aquatic environment may contribute to the distribution, persistence, and fate of hydrophobic organic pollutants such as phenanthrene.[14,15] Phenanthrene is released to the environment *via* several routes, including petrochemical effluents, pipeline leakages, leachates from landfills, and indiscriminate waste disposal.[16]

Adsorption, extraction, bioremediation, chemical oxidation and photocatalytic degradation are the common conventional methods used to remove PAHs present in water.[17] Adsorption has been widely used due to its simplicity, ease of operation, high processing efficiency, and high removal rates for most pollutants.[18] This technique involves the surface accumulation of adsorbate (solute) on the adsorbent (material). The differences in phase composition between the adsorbed phase and

Department of Chemistry, Faculty of Natural and Agricultural Sciences, University of Pretoria, Lynnwood Road, Hatfield, Pretoria 0002, South Africa. E-mail: patricia.forbes@up.ac.za

the bulk fluid phase form the basic principle of separation by adsorption technology. Hence, selecting a suitable adsorption material is a crucial factor influencing PAH adsorption efficiency. Current adsorption materials include activated carbon,[19] zeolites,[20] carbon nanoporous,[21] hydrophobic magnetite,[22] organ bentonite,[23] silica-based mesoporous materials,[24] as well as graphene and its derivatives.[25,26]

These materials have been developed as suitable tools for the remediation of hydrocarbons in aqueous solution without chemical transformation.[27–30] However, graphene and its derivatives have been extensively employed in the adsorption of pollutants from water due to its high surface area, namely 2600 m^2 g^{-1}, tunable surface chemistry, and non-corrosive property.[31–33]

Different forms of graphene include pristine graphene, reduced graphene oxide, graphene nanoshells, graphene oxide and graphene quantum dots (GQDs). In this study, GQDs were chosen as a sorbent of interest and as an alternative to the more commonly used graphene. GQDs could provide several types of interactions with PAHs, such as hydrophobic, π–π stacking, and hydrogen bonding.[34–36]

In addition to their quantum confinement and edge effects, doping GQDs could provide more active sites and significantly modify their inherent characteristics, producing new properties and improved functioning.[34] However, there is no report on the use of GQDs as adsorbents for the removal of PAHs from water due to the hydrophilic nature of GQDs, which contradicts the solid–liquid interphase required in an adsorption process. However, GQDs can be modified to achieve hydrophobicity.

This work aimed to synthesise and functionalise hydrophobic graphene quantum dots (GQDs) to remove phenanthrene contamination from water. The role of different moieties and factors, such as initial concentration of phenanthrene, the presence of anions, temperature, and pH on the adsorption capacity of the three novel adsorbents {namely hexadecyl-GQDs
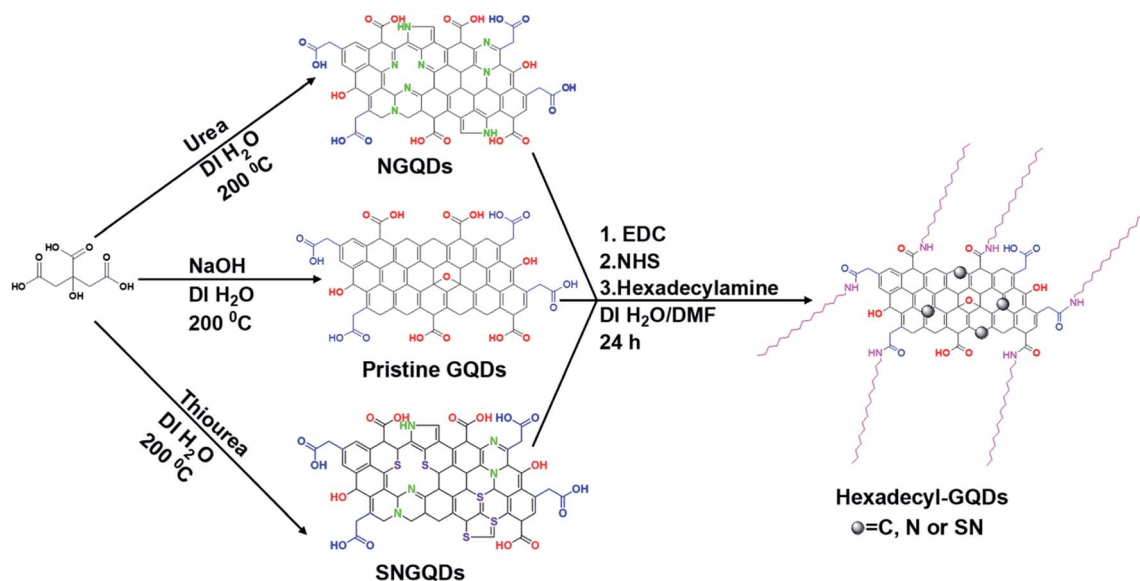
(C_{16}-GQDs), hexadecylamine nitrogen-doped GQDs (C_{16}-NGQDs) and hexadecylamine sulphur and nitrogen co-doped GQDs (C_{16}-SNGQDs)} were evaluated to establish the optimum conditions for efficient water remediation applications.

Results and discussion

Structural elucidation of GQDs and doped GQDs

As shown in Scheme 1, a bottom-up method with good product yield was used to synthesise the hydrophilic GQDs, and a polydispersed particle size distribution was obtained. Hydrophilic GQDs were modified through amide bond formation by coupling –COOH functionalised GQDs with hexadecylamine in a DMF : water mixture (5 : 7) for 24 hours. Centrifugation at 6000 rpm for 20 min in ethanol : water mixture gave the desired products in high yields. These were characterised by transmission electron microscopy (TEM), scanning electron microscopy coupled with energy dispersive X-ray spectroscopy (SEM-EDS), Fourier transform infrared spectroscopy (FTIR), Raman spectroscopy, Brunauer–Emmett–Teller (BET), X-ray photoelectron spectroscopy (XPS) and atomic force microscopy (AFM). The size distribution shown in Fig. 1(c), 2(c) & 3(c) are estimated from TEM images (1(a), 2(a) & 3(a)) via size analysis software (ImageJ).

Fig. 1(a, c), 2(a, c), and 3(a, c) show the TEM images and size distribution histograms of the synthesised GQDs. The TEM images showed the presence of spherical-shaped structures with an average diameter of 10.0, 9.8, and 7.0 nm for C_{16}-GQDs, C_{16}-NGQDs, and C_{16}-SNGQDs, respectively. As shown in Fig. 1(c), 2(c) and 3(c), the size distributions of C_{16}-GQDs, C_{16}-NGQDs, and C_{16}-SNGQDs were in the range of 4–20, 4–25, and 3–15 nm, respectively. Fig. 1(a) reveals the tiny dots aligned diagonally on the TEM grid, while Fig. 2(a) and 3(a) show a spatial distribution of the dots on the grid.

Scheme 1 Preparation and plausible structures of COOH and hexadecylamine functionalised pristine, N-doped, and SN co-doped GQDs.
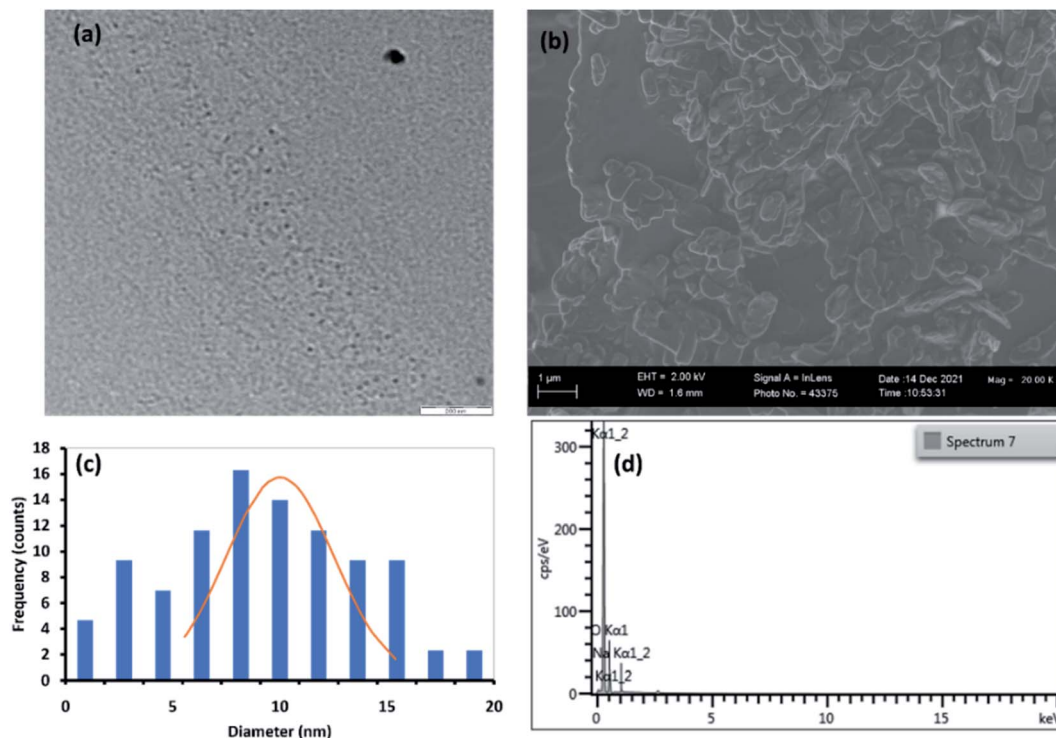
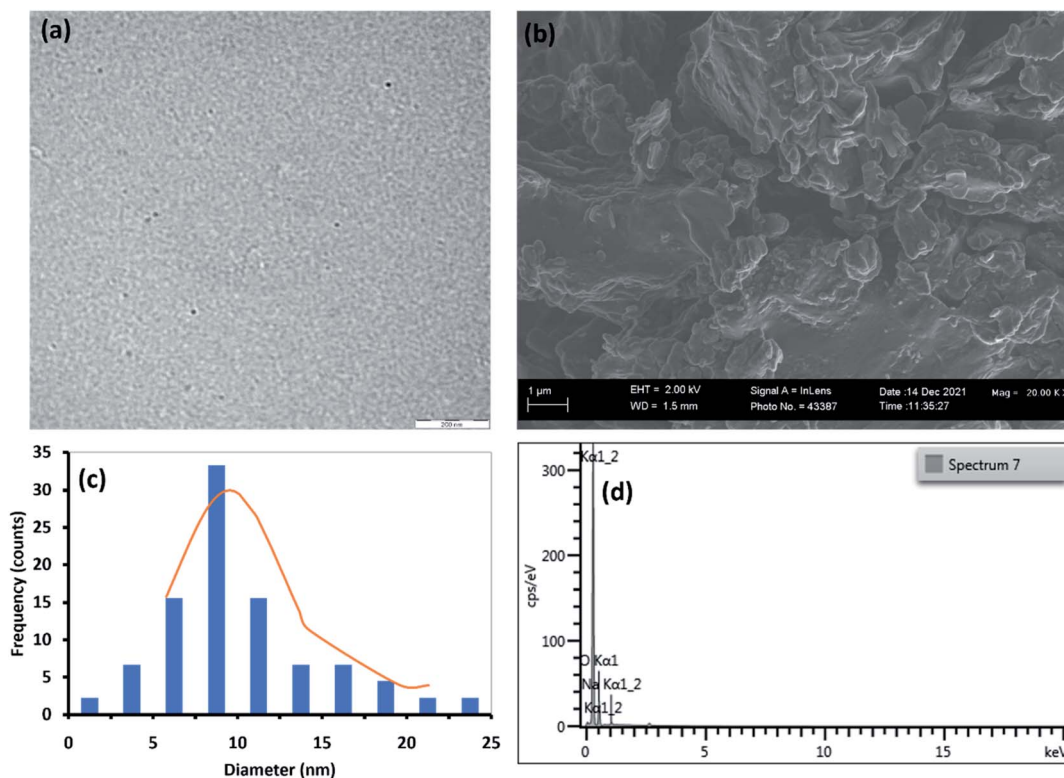**Fig. 1** (a) TEM image, (b) SEM image, (c) particle size distribution and (d) EDS spectrum for C_{16}-GQDs.

Fig. 2 (a) TEM image, (b) SEM image, (c) particle size distribution and (d) EDS spectrum for C_{16}-NGQDs.

From the SEM images (Fig. 1(b), 2(b), and 3(b)), it can be observed that C_{16}-GQDs and C_{16}-NGQDs had a cluster of various shapes, including spherical, sheet, and wrinkled polyhedrons. These clusters consisted of microscopic and larger-sized particles, whereas C_{16}-SNGQDs exhibited similar morphologies with dominantly spherical-like crystals with considerable variation
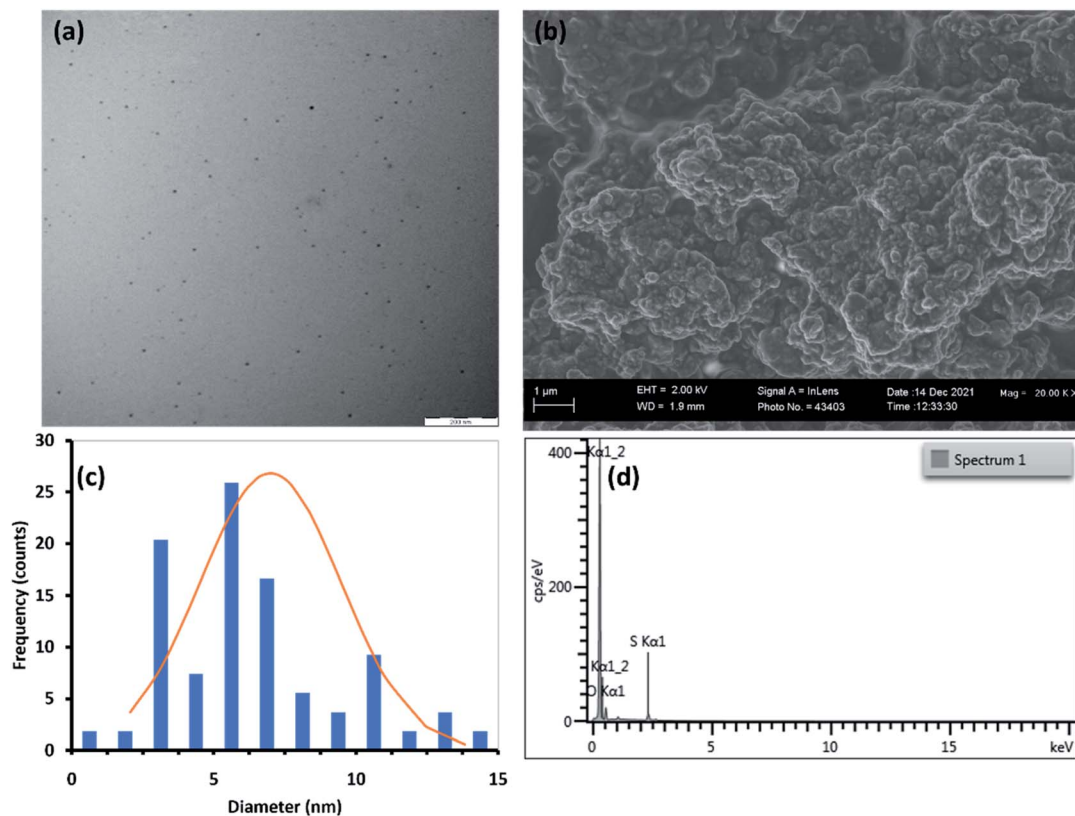
Fig. 3 (a) TEM image, (b) SEM image, (c) particle size distribution and (d) EDS spectrum for C_{16}-SNGQDs.

in particle size, as shown in Fig. 1(b), 2(b) and 3(b). The elemental composition of GQDs was confirmed by EDS, which revealed the presence of C, O, S, N for C_{16}-SNGQDs and C, O, N for C_{16}-NGQDs and C_{16}-GQDs (Fig. 1(d), 2(d) and 3(d)).

The resulting surface moieties and chemical compositions of GQDs were further examined by FTIR. The FTIR spectra of the hexadecylamine functionalised GQDs and hexadecylamine alone are shown in Fig. 4(a). Upon functionalisation of GQDs

with hexadecylamine, the NH_2 peaks in the 3254–3171 cm^{-1} region reduced to one peak corresponding to the NH– stretch, and it appears around 3275 cm^{-1} due to the amide bond formation. Furthermore, the CH_2, CH_3, and C–N from the hexadecylamine appear in the GQDs spectra at 2915–2848, 2956, and 1059–1030 cm^{-1} regions, respectively. C–N corresponds to the amide bond and the nitrogen dopant. Accordingly, C–OH, C=O, C=C, C–O–C, C–C, and –CH=CH– stretches from the
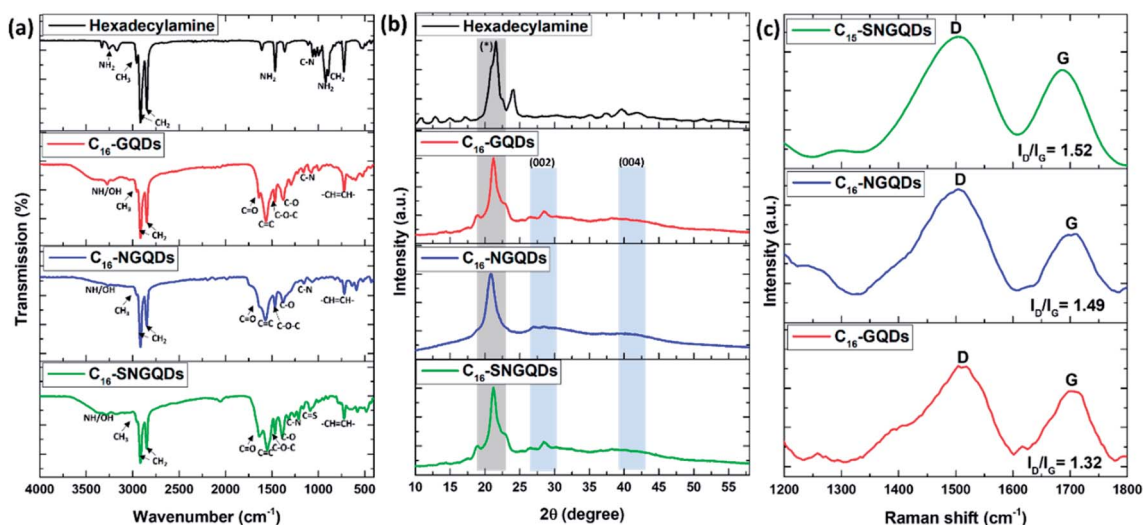

Fig. 4 (a) FTIR spectra, (b) XRD spectra and (c) Raman spectra of hexadecyl-GQDs.
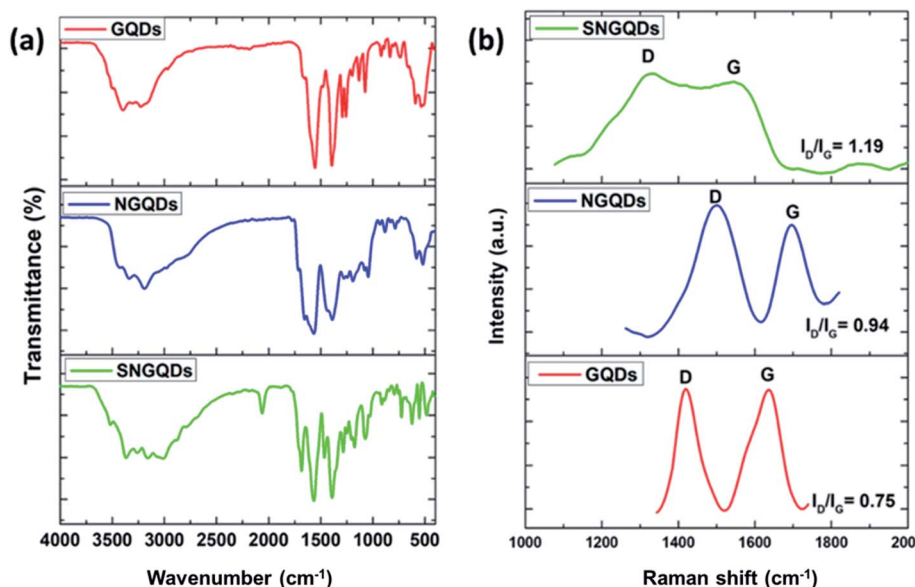
Fig. 5   (a) FTIR and (b) Raman spectra of −COOH functionalised GQDs.

precursor GQDs were observed in the C_{16} composites with the reduction of the C=O peak upon conjugation (Fig. 5(a)). This data reveals that before functionalisation with hexadecylamine, the GQDs were rich in carboxylic groups. However, upon functionalisation, weaker absorption peaks are observed, indicating a decrease of carboxylic group content as expected due to their participation in the amide bond formation. The peak at 1088 cm^{-1} corresponds to C=S from sulphur doping.

XRD and Raman spectroscopy of −COOH and hexadecyl-GQDs were performed to investigate the structural differences further. Fig. 4(b) shows XRD patterns of hexadecyl-GQDs. It can be observed that there are two strong peaks at $\approx 28°$ and $41°$ in the XRD pattern of the hexadecylamine functionalised GQDs, which are characteristic peaks of (002) and (004) of graphite materials, respectively.[37] The peak broadening of the XRD pattern indicates that small nanocrystals are present. The sharp peak at $\approx 21°$ corresponds to the hexadecylamine. A Williamson–Hall plot was used to determine the crystallite size of the functionalised GQDs (eqn (1)).[38]

$$\beta \cos \theta = \frac{k\lambda}{D} + 4\varepsilon \sin \theta \qquad (1)$$

where β is the full width at half maximum (i.e., broadening of the peak) in radians, $k = 0.89$ (ref. 39) is the shape factor, $\lambda = 0.154184$ nm is the wavelength of the X-ray source, D is the crystallite size, θ is the peak position in radians, $\frac{k\lambda}{D}$ is the y-intercept and ε is the gradient. The crystallite size varied from 0.64, 0.49, and 0.62 nm for C_{16}-GQDs, C_{16}-NGQDs, and C_{16}-SNGQDs, respectively.

The chemical composition and elemental binding states were further confirmed by XPS spectroscopy. The wide scan spectra of the hexadecyl-GQDs (Fig. 6(a–k)) show the anticipated presence of C, O and N in the samples with the addition of S in C_{16}-SNGQDs. The high-resolution XPS spectra of C_{16}-SNGQDs

give two peaks for S 2p at 165.8 and 167.3 eV upon deconvolution of the spectra (Fig. 6(b)) attributed to S $2p_{3/2}$ and S $2p_{1/2}$ positions of the −C–S–C− covalent bond of the thiophene-like S due to spin–orbit couplings.[40] Deconvolution of the C 1s high-resolution spectra gave three peaks (Fig. 6(b–e)) attributed to C=C/C–C, C=O/CN and COOH/C=N at ≈ 282, 283 and 285 eV, respectively. Similarly, two peaks for N 1s (Fig. 6(f)) have been obtained due to the presence of an aliphatic N–C bond at 397 eV and primary amino groups (N–H) at 399 eV in the C_{16}-GQDs sample.

In contrast, deconvolution of the C_{16}-NGQDs and C_{16}-SNGQDs gave three peaks at ≈ 396, 397 and 399 eV corresponding to the pyrrolic-N (C–N–C), graphitic-N (or N–C bond) and N–H, respectively. The high-resolution O 1s spectrum showed that the hexadecyl-GQDs contain hydroxyl (≈ 528 eV), carboxyl (≈ 529 eV) and epoxy (≈ 531 eV) groups (Fig. 6(f–k)). A −C–S–C− covalent bond in the S 2p high-resolution spectrum for C_{16}-SNGQDs indicates successful doping with sulphur. Additionally, the detection of the pyrrolic-N and graphitic-N in the high-resolution N 1s spectra suggests that N atoms have been successfully doped into the carbon backbone of GQDs.[40] Moreover, the presence of primary amino groups indicates successful covalent bonding of hexadecylamine with COOH-GQDs.

The Raman spectrum of GQDs (Fig. 4(b) and 5(c)) shows that there were two dominant peaks attributed to the D-band at ca. 1400 cm^{-1} (breathing mode disorder band) and the G-band at ca. 1600 cm^{-1} (tangential vibrational mode). The relative intensity of the disorder D band and the crystalline G band (I_D/I_G) ratio was calculated to determine the relative extent of structural defects in COOH and hexadecylamine functionalised GQDs. Doped GQDs were compared to the pristine GQDs; subsequently, the COOH functionalised GQDs were compared to hexadecylamine functionalised GQDs.
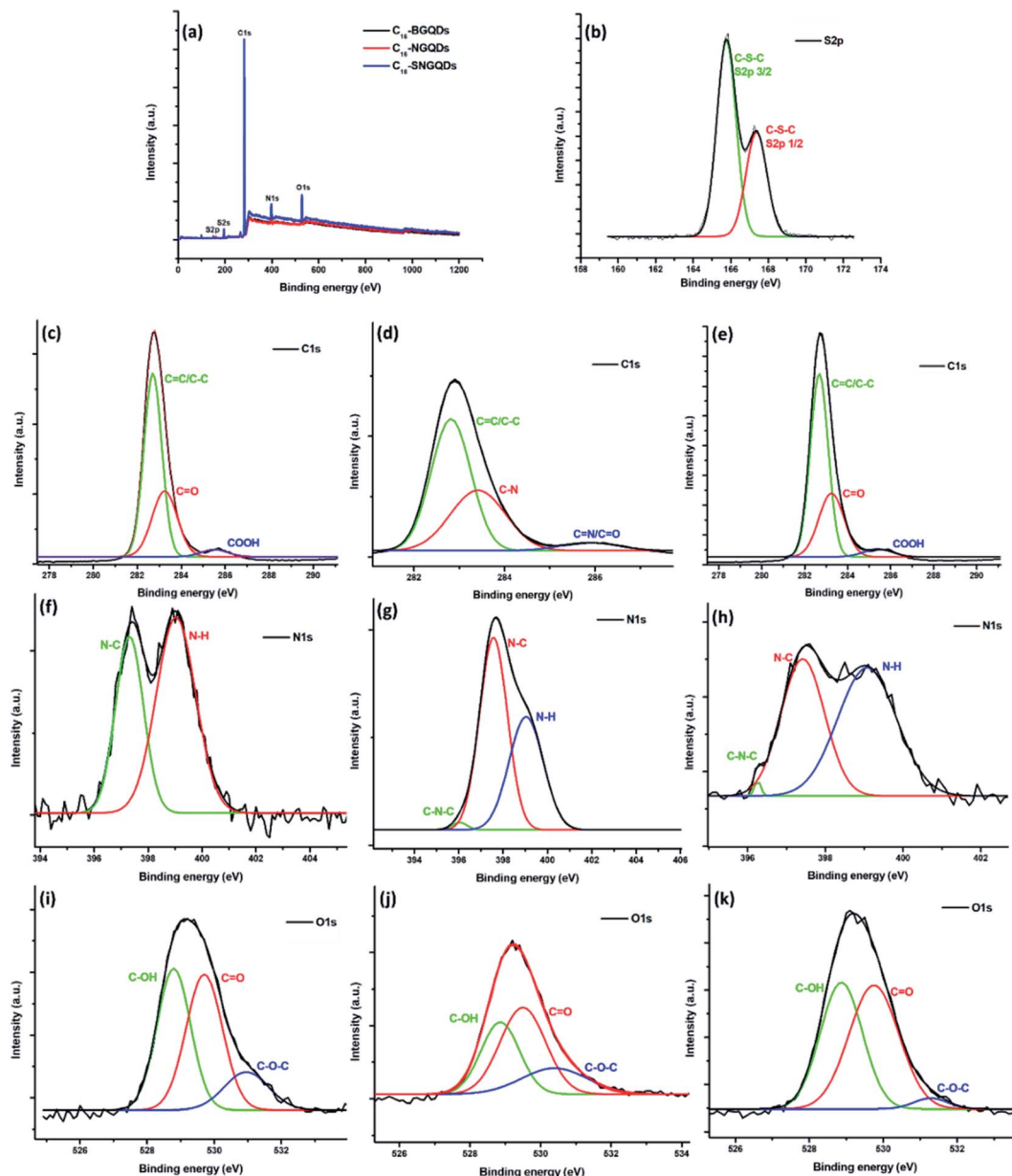
Fig. 6 (a) Wide scan XPS spectra of the hexadecyl-GQDs and (b) high-resolution XPS spectra of C_{16}-SNGQDs showing S 2p band deconvolution. (c–e) C 1s band deconvolution of (c) C_{16}-GQDs, (d) C_{16}-NGQDs, and (e) C_{16}-SNGQDs. (f–h) N 1s band deconvolution of (f) C_{16}-GQDs, (g) C_{16}-NGQDs, and (h) C_{16}-SNGQDs. (i–k) O 1s band deconvolution of (i) C_{16}-GQDs, (j) C_{16}-NGQDs, and (k) C_{16}-SNGQDs.

The D-band was slightly enhanced in the COOH GQDs with the amount of disorder increasing in the order: COOH-GQDs < COOH-NGQDs < COOH-SNGQDs (Fig. 4(b)). This can be attributed to the structural defects introduced to the GQDs by the nitrogen and sulphur dopants in NGQDs and SNGQDs. Furthermore, the introduction of sp^3 hybridised carbons from the hexadecylamine resulted in a more intense D-band and a reduction in the intensity of the G-band, which results from sp^2 hybridised in-plane carbon–carbon bonds. Accordingly, the amount of disorder was increased from 1.32, 1.49 to 1.52 for C_{16}-GQDs, C_{16}-NGQDs, and C_{16}-SNGQDs, respectively (Fig. 5(c)). The significant differences in the Raman spectroscopy of pristine and doped GQDs, as well as before and after

functionalisation with hexadecylamine, are related to the structural changes of these nanomaterials.[41] This could indicate that the GQDs were successfully doped and further functionalised with hexadecylamine.

The 2D band was deconvoluted into four components for C_{16}-GQDs and C_{16}-SNGQDs and five components for C_{16}-NGQDs (Fig. 7). For multilayer graphene, the 2D peak is broader than for a single layer of graphene.[42] Moreover, according to Ndiaye et al.,[43] the I_{2D}/I_G ratio for monolayer, bilayer and multilayer graphene is >2, ≈1 and <0.7, respectively. As shown in Fig. 7(a–c), the ratios of the I_{2D}/I_G peak intensities were 0.018, 0.062 and 0.37 for C_{16}-GQDs, C_{16}-NGQDs, and C_{16}-SNGQDs, respectively, indicative of GQDs with multilayers.
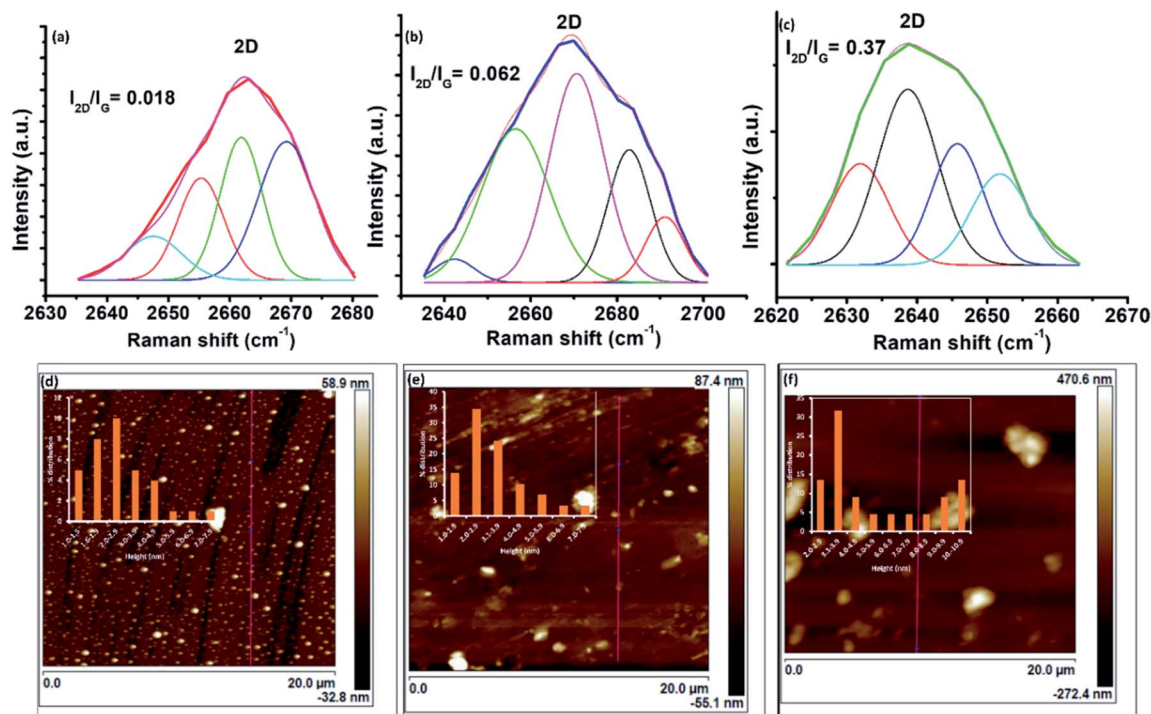
RSC Advances

Paper

Fig. 7 Raman spectra showing a 2D band deconvolution of (a) C_{16}-GQDs, (b) C_{16}-NGQDs, and (c) C_{16}-SNGQDs (above). AFM images of GQDs and their size distribution histograms of (d) C_{16}-GQDs, (e) C_{16}-NGQDs, and (f) C_{16}-SNGQDs. (Insets: histograms showing height distribution) (below).

Furthermore, to determine the number of layers of the hexadecyl-GQDs, AFM analysis was carried out. Fig. 7(d) and (e) shows the AFM images of C_{16}-GQDs, C_{16}-NGQDs, and C_{16}-SNGQDs with insets showing their height distributions. The height measurements were carried out at multiple points covering the entire topography of the image. The bright spots indicate the nanosized hexadecyl-GQDs, and increased clustering is observed for C_{16}-NGQDs, and C_{16}-SNGQDs compared to the undoped GQDs (C_{16}-GQDs). This clustering can be attributed to the number of layers formed by these GQDs. The line profile measurements for these samples were obtained using the NanoScope software tool. This analysis showed that C_{16}-GQDs (Fig. 7(d)) had an average height of 2.9 nm ranging between 1–6 nm, corresponding to dominantly 5 or 6 layers. In contrast, the average heights for C_{16}-NGQDs, and C_{16}-SNGQDs observed were 3.1 and 6.2 nm corresponding to 6 and 12 layers, respectively. Fig. 7(e) and (f) insets show that the height distribution ranged from 1–7 nm for C_{16}-NGQDs and 2–10 nm for C_{16}-SNGQDs. The results showed an increase in average height with the increase in surface functionalisation through doping. These results supported the formation of multilayered GQDs as determined by the 2D analysis in the Raman spectra.

The adsorbance of type I isotherms increases rapidly at low relative pressures (P/P_0), and it slows down at moderate pressure, thus revealing the adsorbent has micropores and mesopores.

Fig. 8 and Table 1 show the spectra data obtained for C_{16}-GQDs, C_{16}-NGQDs and C_{16}-SNGQDs before and after the

adsorption of phenanthrene *via* π–π stacking interactions. Upon adsorption, the I_D/I_G ratio for C_{16}-GQDs increased due to surface modification by phenanthrene. In contrast, there was a decrease in the I_D/I_G ratio for C_{16}-NGQDs and C_{16}-SNGQDs. The reduction in I_D/I_G ratio for C_{16}-NGQDs and C_{16}-SNGQDs can be attributed to the presence of heteroatoms in the graphene sheet and how this affects the interaction with phenanthrene. In addition to the G and D bands, C_{16}-GQDs, C_{16}-NGQDs and C_{16}-SNGQDs have another dominant peak arising from the G + D band (a defect-induced double resonance "inter-valley"
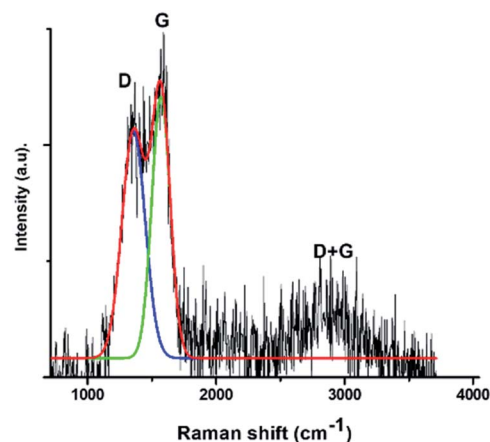

Fig. 8 A representative Raman spectrum of the hexadecyl-GQDs upon adsorption of phenanthrene.

Table 1 Raman spectroscopy properties (cm^{-1}) of the hexadecyl-GQDs before and after adsorption of phenanthrene

	C_{16}-GQDs	$^a C_{16}$-GQDs-Phe	C_{16}-NGQDs	$^a C_{16}$-NGQDs-Phe	C_{16}-SNGQDs	$^a C_{16}$-SNGQDs-Phe
D-band	1509	1416	1495	1412	1498	1358
G-band	1701	1591	1707	1594	1687	1571
2D-band	2662	—	2669	—	2639	—
G + D	2910	2885	2932	2894	2961	2891
I_D/I_G ratio	1.32	1.41	1.49	1.15	1.52	1.10
I_{2D}/I_G ratio	0.018	0.013	0.062	0.042	0.37	0.21

^{a} Phe = phenanthrene.

scattering process)[44,45] at *ca.* 2900 cm^{-1} (a C–H stretch band).[46] Since the D and G + D bands arise from sp^3 hybridised carbons, their presence can be assigned to structural defects. The slight decrease of D band intensity upon adsorption for C_{16}-NGQDs and C_{16}-SNGQDs indicates that the materials become less defective and more crystalline. An opposite trend was observed in the case of C_{16}-GQDs. The significant differences in the Raman spectroscopy before and after adsorption is related to the structural changes of C_{16}-GQDs, C_{16}-NGQDs and C_{16}-SNGQDs.[41] The D, G and the D + G bands of these nanomaterials redshifted upon adsorption of phenanthrene. The redshift, in particular of the G band, according to Yan *et al.*,[46] is caused by the mechanical compression of these materials by phenanthrene.

The BET method was employed to measure the surface area of the material (Fig. 9(a)) and porosity (Fig. 9(b)). The BET results showed a high surface area for C_{16}-SNGQDs of 0.9856 m^2 g^{-1}, whereas, for C_{16}-NGQDS and C_{16}-GQDs, the surface area was found to be 0.4021 and 0.3364 m^2 g^{-1}, respectively. The doping of the graphene quantum dots with sulphur and nitrogen significantly enhanced the surface area. The porosity of the material measured in pore volume was 0.0006, 0.0007 and 0.0017 cm^3 for C_{16}-GQDs, C_{16}-NGQDs and C_{16}-SNGQDs, respectively. For adsorption processes, large specific surface area and pore volume are advantageous. The pattern of the adsorption curves demonstrates type 1 adsorption isotherms for C_{16}-GQDs and C_{16}-NGQDs, increasing fast at low relative pressures (P/P_0) and slowing down at intermediate pressure, which is characteristic of micropore and mesopore adsorbents.

On the contrary, the isotherm for C_{16}-SNGQDs exhibits a type IV adsorption which reflects an adsorbent with a developed micropore and mesopore structure.

Adsorption isotherms

Adsorption isotherms aid with the determination of the nature of the interaction between solutes and adsorbents, adsorption capacities, binding strength, amount of adsorbate adsorbed, and the amount not adsorbed post-equilibration.[30,47] Several adsorption isotherm models, including Linear (eqn (2)), Freundlich (eqn (3)), Langmuir (eqn (4)), and Sips model (eqn (5)) were employed to extrapolate experimental sorption data (Fig. 10). The sum of squared errors (SSE) (eqn (5)) was utilised to validate all adsorption models.[48,49]
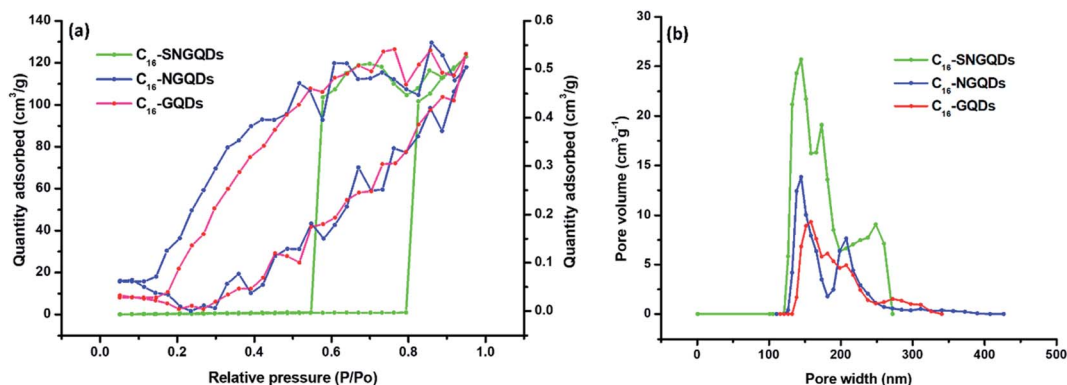
$$q_e = K_d C_e \qquad (2)$$

$$q_e = K_F C_e^N \qquad (3)$$

$$q_e = \frac{q_{max} K_L C_e}{1 + K_L C_e} \qquad (4)$$

$$q_e = \frac{q_m K_s C_e^{m_s}}{1 + K_s \times C_e^{m_s}} \qquad (5)$$

$$\sum_{i=1}^{n} \left(q_{e,cal} - q_{e,exp} \right)_i^2 \qquad (6)$$

where K_F (mg g^{-1}) (L mg^{-1})^N and N are the Freundlich constant and intensity parameter, which describe multilayer sorption

Fig. 9 (a) N_2 adsorption/desorption isotherms and (b) density functional theory (DFT) pore size distributions of hexadecyl-GQDs.
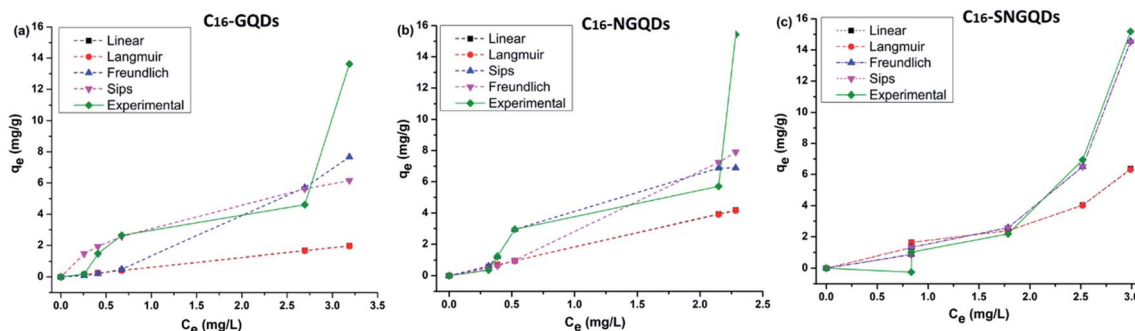
Fig. 10 Phenanthrene sorption isotherm plots for the equilibrium interaction with pristine and functionalized graphene quantum dots (GQDs) (experimental conditions: phenanthrene concentration = 0.5–10 mg L^{-1}; dosage = 5 mg per 10 mL, agitation rate = 200 rpm, $T = 25 \pm 1$ °C, contact time: 24 hours).

capacity and heterogeneity indices; q_{max} (mg g^{-1}) and K_L (L mg^{-1}) are the Langmuir monolayer sorption capacity and constant associated with solute–surface interaction energy, respectively; K_s (L mg^{-1}) and q_{max} (mg g^{-1}) are Sips isotherm model constants, and maximum sorption capacity are Sips isotherm model constants and maximum sorption capacity, and m_s is Sips isotherm exponent; q_e is the amount of solute adsorbed (mg g^{-1}), C_e is the equilibrium non-adsorbed concentration (mg L^{-1}), and K_d (L g^{-1}) is the sorption distribution coefficient.[50]

The nonlinear fitting of multi-parameter models (eqn (2)–(7)) utilised to determine the mechanism and nature of adsorptive interaction between phenanthrene and the synthesised graphene quantum dots were reported to be more accurate than fitting of the linear forms of the models.[51,52] Isotherm data revealed that the Sips isotherm model generally fitted the experimental data best for doped hexadecyl-GQDs (with N and SN) considering the SSE and R^2 values (Table 2). The Sips model is a combination of Freundlich and Langmuir models often used to describe complex adsorption systems.[53,54] Thus,

phenanthrene interaction with C$_{16}$-GQDs is highly heterogeneous, which explains the considerably more significant heterogeneity (N & m_s) index of 2.85 and 8.00, respectively (Table 2). Experimental data tended more towards multilayer adsorption (Freundlich) than monolayer adsorption (Langmuir), considering the R^2 values. The interaction of phenanthrene with GQDs would not be adequately described by single mechanism models like those proposed by Freundlich and Langmuir due to restrictions brought on by a higher adsorbate concentration, physicochemical properties of functionalised GQDs, and the nature of the solute. However, the Sips model could reduce to the Langmuir or Freundlich model subject to changes in concentration of pollutants and surface interactions with the adsorbents.[30,49]

Overall, the Sips maximum sorption capacity (q_m) and adsorption capacities (K_d & K_F) revealed that the introduction of doping agent (N) and co-dopants (SN) enhanced the adsorption performance of the GQDs. This can be attributed to potentially improved surface hydrophobicity due to chemical modifications, as well as smaller particle size and enhanced surface morphology and crystal structure as described in the previous sections.

Effect of hydrochemistry

Effect of solution pH and anionic interferences. Solution pH and the presence of anions/cations influence the adsorption performance of adsorbents towards eliminating hydrophobic organic compounds from aqueous solution.[54,55] Altering the pH of the solution may affect the surface charge of the sorbent and sorbate molecule.[30] The impact of pH variation is more prominent in solutes and sorbents with protonated moieties (–OH, –COOH, –NH$_2$ group, etc.) due to potential protonation and formation of deprotonated groups under variable pH conditions.[48] The extensive modifications and functionalisation described in Scheme 1 evidently included moieties that are sensitive to solution pH. Therefore, the effect of pH was evaluated between the pH range of 2–12 for phenanthrene adsorption by GQDs, as the pH of environmental aqueous systems and wastewater often varies.

The results showed that phenanthrene sorption onto the various graphene quantum dots (GQDs) is favourable under

Table 2 Adsorption isotherm parameters for sorption of phenanthrene onto various functionalised GQDs nano-adsorbents

Sorption models		Adsorption parameters		
		C$_{16}$-GQDs	C$_{16}$-NGQDs	C$_{16}$-SNGQDs
Freundlich	K_F	1.77	2.63	8.66
	N	2.85	0.79	0.79
	SSE	0.66	0.72	0.55
	R^2	0.9000	0.9137	0.9057
Langmuir	q_{max} (mg g^{-1})	0.41	21.93	58.14
	K_L (L mg^{-1})	1×10^{-3}	5×10^{-3}	10×10^{-2}
	SSE	0.87	0.78	0.64
	R^2	0.6247	0.6474	0.7714
Linear	K_d	2.19	2.66	10.12
	SSE	0.87	0.78	0.65
	R^2	0.8993	0.7027	0.9066
Sips	K_s	0.43	0.003	0.006
	q_m (mg g^{-1})	103.0	874.4	1377.1
	m_s	8.00	2.50	0.77
	SSE	0.59	0.72	0.55
	R^2	0.9248	0.9922	0.9679

Paper

acidic pH conditions, similar to an earlier report on graphene wool adsorbent.[30] The modification of hydrophobic GQDs through an amide bond formation by coupling COOH functionalised GQDs with hexadecylamine may facilitate hydrogen bonding under acidic pH, in addition to π–π, hydrophobic and van der Waal's interactions between the sorbates and sorbents.[56] The decrease in adsorption under basic pH may result from electrostatic repulsion between the negatively charged surfaces and the electron-rich π system of phenanthrene complexes (Fig. 11).

The removal of an equimolar concentration of phenanthrene using the hexadecyl-GQDs was investigated in the presence of various anions under similar experimental conditions (Fig. 12). Among the five competing anions used in the study, CO_3^{2-} and Cl^- had the greatest inhibitory influence on the sorption interaction. The order of inhibition followed: carbonate > chloride > nitrate > phosphate > sulfate. The observed trend can be attributed to the difference in the extent to which the anions alter the hydrochemistry (i.e., salinity and pH) of the phenanthrene-contaminated solution. It has been reported that sulfates and phosphates bind strongly with water molecules to create cavities, thus reducing the water molecules available for PAH dissolution. This "salting-out effect" may have facilitated the enhanced adsorption of phenanthrene onto the hydrophobic GQDs in the presence of sulfates and phosphates.[57] However, carbonate salts are moderately strong bases in aqueous solution; $CO_3^{2-} + H_2O \rightleftharpoons HCO_3^- + OH^-$, and alkaline pH does not favour phenanthrene removal.[30]

Effect of temperature. Many physical, chemical and biological processes are significantly influenced by temperature. The van't Hoff equations were used to extrapolate adsorption thermodynamic parameters such as a change in enthalpy ($\Delta H°$), change in entropy ($\Delta S°$), and a variation in Gibbs free energy ($\Delta G°$) (eqn (7) and (8)). Eqn (5) was used to get the adsorption

Fig. 12 Effect of various anions on the adsorption of phenanthrene by hexadecyl-GQDs, $N = 3$. (experimental conditions: phenanthrene concentration = 5.61×10^{-6} M; concentration anions = 0.01 M; adsorbent dosage = 5 mg per 10 mL; agitation rate = 200 rpm, $T = 25 \pm 1$ °C, contact time: 24 hours).

equilibrium constant (b) for different temperatures and the van't Hoff plot (Fig. 13):[53]

$$\ln b = \frac{\Delta S°}{R} - \frac{\Delta H°}{RT} \tag{7}$$

$$\Delta G° = -RT \ln b \tag{8}$$

where $\Delta G°$ represents the change in Gibbs free energy (kJ mol^{-1}), $\Delta H°$ represents enthalpy change (kJ mol^{-1}), $\Delta S°$ represents the entropy change (J mol^{-1} K^{-1}), and R represents the gas constant (8.314 J mol^{-1} K^{-1}). T represents the thermodynamic temperature (K). The Langmuir adsorption constant (K_L), whose value is in L mg^{-1}, is multiplied by 1000 to change the units to L g^{-1} and the molecular weight of phenanthrene molecular weight, as shown in Table 2, to obtain the value of b.
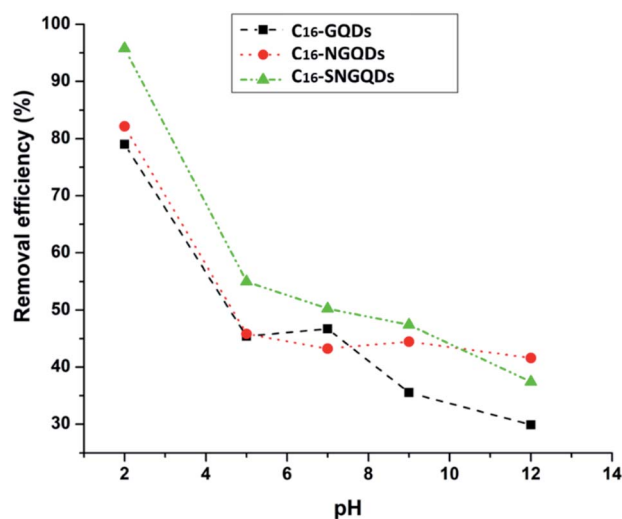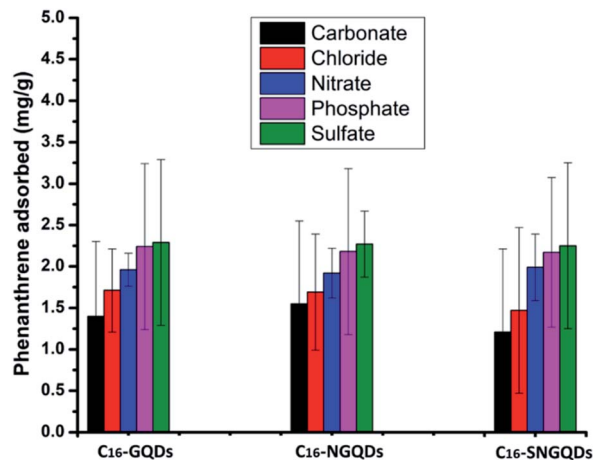

Fig. 11 Effect of pH on the adsorption of phenanthrene by pristine and doped hexadecyl-GQDs (experimental conditions: phenanthrene concentration = 5 mg L^{-1}; dosage = 5 mg per 10 mL, agitation rate = 200 rpm, $T = 25 \pm 1$ °C, contact time: 24 hours).
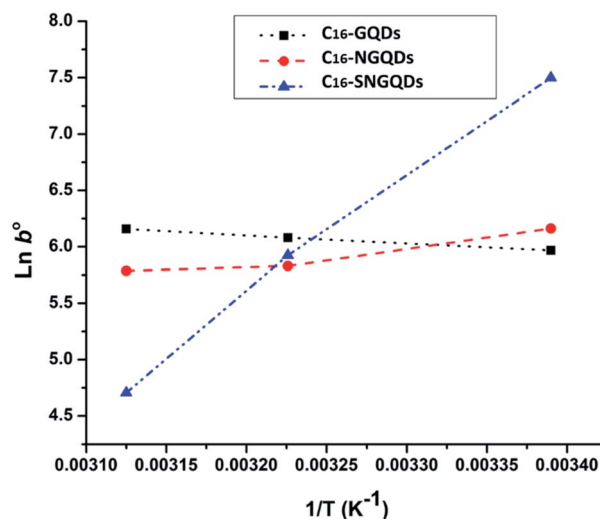

Fig. 13 Van't Hoff plot for phenanthrene adsorption by hexadecyl-GQDs.

Table 3 Thermodynamic parameters for sorption of phenanthrene onto pristine and doped hexadecyl-GQDs

Sorbent	Temperature (K)	ln b	ΔG° (kJ mol^{-1})	ΔH° (kJ mol^{-1})	ΔS° (kJ mol^{-1} K^{-1})
	298	5.97	−14.79		
C_{16}-GQDs	313	6.08	−15.82	6.10	0.07
	323	6.16	−16.54		
	298	6.16	−16.54		
C_{16}-NGQDs	313	5.83	−15.17	−12.47	0.01
	323	5.79	−15.55		
C_{16}-SNGQDs	298	7.50	−18.58		
	313	5.93	−15.43	−88.61	−0.24
	323	4.71	−12.65		

Phenanthrene sorption by hexadecyl-GQDs is an endothermic interaction (+ΔH°), while interaction with N-doped and SN-doped hexadecyl-GQDs is exothermic −ΔH° (Table 3). The negative G° confirms a spontaneous adsorption process, and spontaneity increased from 25 to 50 °C. Table 3 revealed that temperature significantly influenced the adsorption capacity (b) of C_{16}-SNGQDs (1804 L g^{-1} @25 °C to 111 L g^{-1} @50 °C), in contrast to C_{16}-NGQDs (474 L g^{-1} @25 °C to 326 L g^{-1} @50 °C) and C_{16}-GQDs (390 L g^{-1} @25 °C to 472 L g^{-1} @50 °C). An increase in temperature enhanced the adsorption of phenanthrene by C_{16}-GQDs, being an endothermic process similar to an earlier report on phenanthrene adsorption by graphene wool.[30] However, the reverse is the case for C_{16}-NGQDs and C_{16}-SNGQDs, as they revealed spontaneous exothermic interactions with the adsorbate. The modification of C_{16}-GQDs, such that higher adsorption efficiency is potentially obtainable at lower temperature regimes, is eco-friendly and cost-effective in terms of process economics.

Experimental

Materials

Citric acid, thiourea, urea, hexadecylamine, 1-ethyl-3-(3-dimethylaminopropyl)carbodiimide (EDC), *N*-hydroxysuccinimide (NHS), anhydrous dimethylformamide (DMF), and 0.22 μm pore size syringe filters containing a hydrophilic polyethersulfone (PES) membrane were purchased from Merck. Ethanol (EtOH), sodium hydroxide, ammonia, hydrochloric acid, and calcium chloride were purchased from Associated Chemical Enterprises (South Africa). Phenanthrene (PHE) standard (≥98% purity) was purchased from Supelco. Deionised water (DI, 9.2 μS cm^{-3}) from a Milli-Q water purification system (Millipore, Bedford, MA, USA) was employed to prepare all the solutions. SnakeSkin™ 3.5 kDa MCOW dialysis tubing was purchased from Thermo Fisher Scientific (South Africa).

Synthesis and functionalisation of graphene quantum dots (GQDs)

Synthesis of COOH functionalised GQDs. The GQDs were synthesised by modifying a method that has been described previously.[58,59] Briefly, 1 g citric acid was heated directly on a hotplate at 200 °C in a 100 mL beaker until it changed to an orange liquid (≈10 min), 80 mL of deionised (DI) water was added, and the solution and was stirred for 30 min and sonicated for another 30 min, then adjusted with 0.1 M NaOH solution to pH 8.0. The solution was filtered through a 0.22 μm microporous membrane, then treated with a 3.5 kDa MCOW dialysis tube for 5 h and freeze-dried for 48 h. Light-yellow solid carboxylic functionalised GQDs were obtained in ≈0.50 g.

For the synthesis of N doped and SN co-doped GQDs, 1.0 g of citric acid was placed with 1.751 g urea and 2.375 g of thiourea separately at a 1 : 3 (citric acid: dopant) molar ratio in a beaker, and the same procedure as above was followed. Brown-yellow solids were obtained in ≈0.5 g for NGQDs and SNGQDs, respectively.

Synthesis of hexadecylamine functionalised GQDs. The hydrophobic GQDs were synthesised by modifying a method that has been described previously,[60] as shown in Scheme 1. Briefly, ≈0.5 g of COOH-GQDs, COOH-NGQDs, and COOH-SNGQDs were dissolved in separate vials in 3 mL DI water. A 2 mL solution of EDC (0.0776 g, 0.1 M) followed by a 2 mL solution of NHS (0.0575 g, 0.1 M) in DI water was added to the COOH-GQDs solutions at room temperature for 2 h to activate the COOH groups. Subsequently, ≈1.0 g of hexadecylamine added to 5 mL DMF was heated to make a solution and was quickly added to the COOH-GQDs solutions. The mixtures were further stirred for 24 h. The resulting conjugates (C_{16}-GQDs, C_{16}-NGQDs, and C_{16}-SNGQDs) were centrifuged for 20 min at 6000 rpm, and the precipitates were washed with an ethanol : water (50 : 50) mixture to ensure that unreacted GQDs and hexadecylamine were eliminated. Finally, 80% ethanol solution was used for washing, and the solids were left to dry in a vacuum drier at 40 °C overnight to obtain 1.234, 1.254 and 1.284 g of C_{16}-GQDs, C_{16}-NGQDs, and C_{16}-SNGQDs, respectively.

Characterisation of graphene quantum dots adsorbent. The morphological and structural elucidation of the COOH- and hexadecylamine functionalised GQDs were carried out by advanced techniques, which include Raman spectroscopy (WITec alpha300 RAS+ confocal Raman microscope, WiTec, Germany) operated at a low-power laser (5 mW) and excitation wavelength of 532 nm. An energy-dispersive X-ray spectrometer (EDS) coupled with a Zeiss Ultra-Plus 55 field emission scanning electron microscope (FE-SEM) was used for scanning electron microscopy (OXFORD Link-ISIS-300 Zeiss, Germany). High-resolution transmission electron microscopy (TEM) images of GQDs were obtained using a JEOL JEM 2100F (JOEL Ltd, Tokyo,

Japan) operated at 200 kV. Powder X-ray diffraction (XRD) patterns were obtained using a Bruker D2 Phaser, Cu (Kα) radiation ($\lambda = 1.54184$ Å) (Bruker AXS GmbH, Karlsruhe, Germany). FTIR spectra were obtained using a Bruker Alpha-T spectrometer (Bruker Optik GmbH, Ettlingen, Germany). Using an Al (monochromatic) anode with a charge neutraliser and an AXIS Ultra DLD (provided by Kratos Analytical), an XPS examination was performed. The Quantachrome TouchWin™ software analyser on the NOVA Touch LX6 version was used to measure the nitrogen adsorption and desorption isotherms. All samples were degassed in a high vacuum atmosphere at 50 °C for 10 hours. BET method was used to compute the specific surface area from the adsorption isotherms in the relative pressure range (P/P_0) of 0.01 to 0.2, and the DFT approach was used to determine the pore size distribution. The surface morphologies and roughness analyses were characterised by Veeco Nanoman V Atomic force microscopy (AFM), using image data acquired at a scan rate of 2.441 Hz and scan size of 20 μm × 20 μm in tapping mode. NanoScope software was used to determine the height of the hexadecyl-GQDs.

Adsorption isotherm experiments. Batch adsorption of phenanthrene by hexadecyl-GQDs was performed in 40 mL PTFE screw cap amber vials (Stargate Scientific, South Africa) at 25 ± 1 °C. Background electrolyte contained 0.01 mol L^{-1} CaCl$_2$ in DI water with 200 mg L^{-1} of NaN$_3$ to inhibit microbial activity. The isotherm experiment was conducted with initial phenanthrene concentrations ranging from 0.5 to 10 mg L^{-1}. Thermodynamic evaluations were conducted between 25 and 50 °C using a thermostated shaking water bath (Wisebath, Celsius Scientific, South Africa). The effect of anions on the adsorption of an equivalent concentration of phenanthrene was studied using background electrolytes composed of 0.01 M of NaCl, NaNO$_3$, Na$_2$SO$_4$, NaHCO$_3$, and Na$_2$HPO$_4$. These sodium salts were selected to remove the effect of index cation.[61] The effect of pH on the adsorption of phenanthrene was evaluated for a pH range of 2 to 12 by pH adjustments using 0.1 M NaOH or HCl, respectively.[53]

Quantification. After the equilibration period, the vials were centrifuged at 6000 rpm for 5 min prior to the collection of clear supernatants. The phenanthrene concentrations were determined in triplicate ($n = 3$) using fluorescence spectroscopy at an excitation wavelength of 290 nm and emission at 300 nm (Horiba Jobin Yvon Fluoromax-4 spectrofluorometer). The regression coefficients (R^2) of matrix-matched calibration curves were obtained in the phenanthrene concentration range of 0.5–10 mg L^{-1}. The equilibrium concentration (C_e, mg L^{-1}) and solute adsorbed (q_e, mg g^{-1}) were determined using the calibration regression equation and mass-balance equation, respectively:[53,62]

$$q_e = \frac{(C_0 - C_e)V_0}{S_m} \quad (9)$$

where V_0 is the initial volume (L), S_m is the mass (g) of the adsorbent, C_0 is the initial concentration (mg L^{-1}), and C_e is the equilibrium solute concentration (mg L^{-1}).

$$\text{Removal efficiency } (\%) = \frac{(C_0 - C_e)}{C_0} \times 100 \quad (10)$$

Conclusions

The solubility of GQDs facilitates its application as a chemical sensor in water but limits its application as nano-adsorbent for the removal of chemical pollutants in aqueous media. This study addressed this challenge by successfully producing insoluble and nanostructured GQDs *via* facile chemical modification. Three novel hexadecyl-GQDs with varying moieties on the surface were synthesised as adsorbents to examine the effect of surface functionalisation on their adsorption capacity. The use of dopants, such as nitrogen and sulphur, has been applied in the development of nanomaterials to enhance the morphology and physicochemical properties of various adsorbents in the past. In this study, detailed structural elucidation revealed improved crystalline structure, smaller particle size distribution, and the presence of functional groups, which enhances sorbate–sorbent interactions. The adsorption performance observed in this study follows the trend; C$_{16}$-SNGQDs > C$_{16}$-NGQDs > C$_{16}$-GQDs (pristine), and these nanostructured materials are best utilised at ambient temperature and acidic pH range. Therefore, co-doping with nitrogen and sulphur groups and modification of hydrophilic GQDs to the hydrophobic form enhances their physicochemical properties and adsorption performance. The modification of C$_{16}$-GQDs, such that higher adsorption efficiency is potentially obtainable at lower temperature regimes, is eco-friendly and cost-effective. Therefore, with appropriate fabrication, functionalised GQDs are potentially suitable adsorbents for the removal of organic micro-pollutants from water.

Author contributions

Gugu Kubheka: conceptualisation, formal analysis, investigation, methodology, writing-original draft, visualisation, funding acquisition. Adedapo Adeola: formal analysis, investigation, methodology, writing-original draft, visualisation. Patricia Forbes: funding acquisition, project administration, resources, supervision, validation.

Conflicts of interest

There are no conflicts to declare.

Acknowledgements

References

1 J. Wang, X. Liu, G. Liu, Z. Zhang, H. Wu, B. Cui, J. Bai and W. Zhang, Size effect of polystyrene microplastics on sorption of phenanthrene and nitrobenzene, *Ecotoxicol. Environ. Saf.*, 2019, **173**, 331–338.

2 Z. Wang, J. Chen, P. Yang, F. Tian, X. Qiao, H. Bian and L. Ge, Distribution of PAHs in pine (Pinus thunbergii) needles and soils correlates with their gas-particle partitioning, *Environ. Sci. Technol.*, 2009, **43**(5), 1336–1341.

3 M. Qiao, Y. Bai, W. Cao, Y. Huo, X. Zhao, D. Liu and Z. Li, Impact of secondary effluent from wastewater treatment plants on urban rivers: polycyclic aromatic hydrocarbons and derivatives, *Chemosphere*, 2018, **211**, 185–191.

4 Z. A. ALOthman, A. Y. Badjah and I. Ali, Facile synthesis and characterization of multi walled carbon nanotubes for fast and effective removal of 4-tert-octylphenol endocrine disruptor in water, *J. Mol. Liq.*, 2019, **275**, 41–48.

5 M. Pogorzelec and K. Piekarska, Application of semipermeable membrane devices for long-term monitoring of polycyclic aromatic hydrocarbons at various stages of drinking water treatment, *Sci. Total Environ.*, 2018, **631**, 1431–1439.

6 H. K. Bojes and P. G. Pope, Characterization of EPA's 16 priority pollutant polycyclic aromatic hydrocarbons (PAHs) in tank bottom solids and associated contaminated soils at oil exploration and production sites in Texas, *Regul. Toxicol. Pharmacol.*, 2007, **47**(3), 288–295.

7 M. Kalantari, J. Zhang, Y. Liu and C. Yu, Dendritic mesoporous carbon nanoparticles for ultrahigh and fast adsorption of anthracene, *Chemosphere*, 2019, **215**, 716–724.

8 W. Fu, M. Xu, K. Sun, L. Hu, W. Cao, C. Dai and Y. Jia, Biodegradation of phenanthrene by endophytic fungus Phomopsis liquidambari in vitro and in vivo, *Chemosphere*, 2018, **203**, 160–169.

9 A. Rubio-Clemente, R. A. Torres-Palma and G. A. Peñuela, Removal of polycyclic aromatic hydrocarbons in aqueous environment by chemical treatments: a review, *Sci. Total Environ.*, 2014, **478**, 201–225.

10 W. Guo, B. Pan, S. Sakkiah, G. Yavas, W. Ge, W. Zou, W. Tong and H. Hong, Persistent organic pollutants in food: contamination sources, health effects and detection methods, *Int. J. Environ. Res. Public Health*, 2019, **16**(22), 4361.

11 I. Martorell, G. Perelló, R. Martí-Cid, V. Castell, J. M. Llobet and J. L. Domingo, Polycyclic aromatic hydrocarbons (PAH) in foods and estimated PAH intake by the population of Catalonia, Spain: temporal trend, *Environ. Int.*, 2010, **36**(5), 424–432.

12 H. I. Abdel-Shafy and M. S. Mansour, A review on polycyclic aromatic hydrocarbons: source, environmental impact, effect on human health and remediation, *Egypt. J. Pet.*, 2016, **25**(1), 107–123.

13 A. Mojiri, J. L. Zhou, A. Ohashi, N. Ozaki and T. Kindaichi, Comprehensive review of polycyclic aromatic hydrocarbons in water sources, their effects and treatments, *Sci. Total Environ.*, 2019, **696**, 133971.

14 A. O. Adeola and P. B. C. Forbes, Influence of natural organic matter fractions on PAH sorption by stream sediments and a synthetic graphene wool adsorbent, *Environ. Technol. Innovation*, 2021, **21**, 101202.

15 W. Liu, Z. Cai, X. Zhao, T. Wang, F. Li and D. Zhao, High-capacity and photoregenerable composite material for efficient adsorption and degradation of phenanthrene in water, *Environ. Sci. Technol.*, 2016, **50**(20), 11174–11183.

16 I. A. Ololade, B. O. Adetiba, F. F. Oloye, O. O. Ololade, N. A. Oladoja, S. B. Obadawo, M. M. Anifowose, T. A. Akinnifesi, D. Akerele and A. B. Alabi, Bioavailability of polycyclic aromatic hydrocarbons (PAHs) and Environmental Risk (ER) Assessment: The case of the Ogbese river, Nigeria, *Reg. Stud. Mar. Sci.*, 2017, **9**, 9–16.

17 R. Crisafully, M. A. L. Milhome, R. M. Cavalcante, E. R. Silveira, D. De Keukeleire and R. F. Nascimento, Removal of some polycyclic aromatic hydrocarbons from petrochemical wastewater using low-cost adsorbents of natural origin, *Bioresour. Technol.*, 2008, **99**(10), 4515–4519.

18 T. Sasaki and S. Tanaka, Adsorption behavior of some aromatic compounds on hydrophobic magnetite for magnetic separation, *J. Hazard. Mater.*, 2011, **196**, 327–334.

19 L. Augulyte, D. Kliaugaite, V. Racys, D. Jankunaite, A. Zaliauskiene, P.-A. Bergqvist and P. L. Andersson, Multivariate analysis of a biologically activated carbon (BAC) system and its efficiency for removing PAHs and aliphatic hydrocarbons from wastewater polluted with petroleum products, *J. Hazard. Mater.*, 2009, **170**(1), 103–110.

20 J. Lemić, M. Tomašević-Čanović, M. Adamović, D. Kovačević and S. Milićević, Competitive adsorption of polycyclic aromatic hydrocarbons on organo-zeolites, *Microporous Mesoporous Mater.*, 2007, **105**(3), 317–323.

21 L. Ai, C. Zhang and Z. Chen, Removal of methylene blue from aqueous solution by a solvothermal-synthesized graphene/magnetite composite, *J. Hazard. Mater.*, 2011, **192**(3), 1515–1524.

22 Y. Tang, H. Guo, L. Xiao, S. Yu, N. Gao and Y. Wang, Synthesis of reduced graphene oxide/magnetite composites and investigation of their adsorption performance of fluoroquinolone antibiotics, *Colloids Surf., A*, 2013, **424**, 74–80.

23 Z. Wu and L. Zhu, Removal of polycyclic aromatic hydrocarbons and phenols from coking wastewater by simultaneously synthesized organobentonite in a one-step process, *J. Environ. Sci.*, 2012, **24**(2), 248–253.

24 C. B. Vidal, A. L. Barros, C. P. Moura, A. C. De Lima, F. S. Dias, L. C. Vasconcellos, P. B. Fechine and R. F. Nascimento, Adsorption of polycyclic aromatic hydrocarbons from aqueous solutions by modified periodic mesoporous organosilica, *J. Colloid Interface Sci.*, 2011, **357**(2), 466–473.

25 V. Chabot, D. Higgins, A. Yu, X. Xiao, Z. Chen and J. Zhang, A review of graphene and graphene oxide sponge: material synthesis and applications to energy and the environment, *Energy Environ. Sci.*, 2014, **7**(5), 1564–1596.

26 A. Khan, J. Wang, J. Li, X. Wang, Z. Chen, A. Alsaedi, T. Hayat, Y. Chen and X. Wang, The role of graphene oxide and graphene oxide-based nanomaterials in the removal of pharmaceuticals from aqueous media: a review, *Environ. Sci. Pollut. Res.*, 2017, **24**(9), 7938–7958.

27 Z. Wu, Z. Sun, P. Liu, Q. Li, R. Yang and X. Yang, Competitive adsorption of naphthalene and phenanthrene on walnut

shell based activated carbon and the verification via theoretical calculation, *RSC Adv.*, 2020, **10**(18), 10703–10714.

28 K. Yang, B. Chen and L. Zhu, Graphene-coated materials using silica particles as a framework for highly efficient removal of aromatic pollutants in water, *Sci. Rep.*, 2015, **5**(1), 1–12.

29 A. O. Adeola, A. S. Akingboye, O. T. Ore, O. A. Oluwajana, A. H. Adewole, D. B. Olawade and A. C. Ogunyele, Crude oil exploration in Africa: socio-economic implications, environmental impacts, and mitigation strategies, *Environ. Syst. Decis.*, 2021, 1–25.

30 A. O. Adeola and P. B. C. Forbes, Optimization of the sorption of selected polycyclic aromatic hydrocarbons by regenerable graphene wool, *Water Sci. Technol.*, 2019, **80**(10), 1931–1943.

31 F. Perreault, A. F. De Faria and M. Elimelech, Environmental applications of graphene-based nanomaterials, *Chem. Soc. Rev.*, 2015, **44**(16), 5861–5896.

32 J. Xu, Z. Cao, Y. Zhang, Z. Yuan, Z. Lou, X. Xu and X. Wang, A review of functionalized carbon nanotubes and graphene for heavy metal adsorption from water: Preparation, application, and mechanism, *Chemosphere*, 2018, **195**, 351–364.

33 W. Peng, H. Li, Y. Liu and S. Song, A review on heavy metal ions adsorption from water by graphene oxide and its composites, *J. Mol. Liq.*, 2017, **230**, 496–504.

34 J. Gu, M. Hu, Q. Guo, Z. Ding, X. Sun and J. Yang, High-yield synthesis of graphene quantum dots with strong green photoluminescence, *RSC Adv.*, 2014, **4**(91), 50141–50144.

35 T. Yamamoto, T. Noguchi and K. Watanabe, Edge-state signature in optical absorption of nanographenes: tight-binding method and time-dependent density functional theory calculations, *Phys. Rev. B*, 2006, **74**(12), 121409.

36 H. Abdelsalam, T. Espinosa-Ortega and I. Luk'yanchuk, Electronic and magnetic properties of graphite quantum dots, *Low Temp. Phys.*, 2015, **41**(5), 396–400.

37 Z. Li, C. Lu, Z. Xia, Y. Zhou and Z. Luo, X-ray diffraction patterns of graphite and turbostratic carbon, *Carbon*, 2007, **45**(8), 1686–1695.

38 A. Narjis, H. El Aakib, M. Boukendil, M. El Hasnaoui, L. Nkhaili, A. Aberkouks and A. Outzourhit, Controlling the structural properties of pure and aluminum doped zinc oxide nanoparticles by annealing, *J. King Saud Univ., Sci.*, 2020, **32**(1), 1074–1080.

39 U. Holzwarth and N. Gibson, The Scherrer equation versus the "Debye-Scherrer equation", *Nat. Nanotechnol.*, 2011, **6**(9), 534.

40 Z. Yan, Z. Qu, X. Niu, C. Tian, C. Fan and B. Ye, A green synthesis of highly fluorescent nitrogen-doped graphene quantum dots for the highly sensitive and selective detection of mercury (II) ions and biothiols, *Anal. Methods*, 2016, **8**(7), 1565–1571.

41 V. Datsyuk, M. Kalyva, K. Papagelis, J. Parthenios, D. Tasis, A. Siokou, I. Kallitsis and C. Galiotis, Chemical oxidation of multiwalled carbon nanotubes, *Carbon*, 2008, **46**(6), 833–840.

42 K. M. Wibowo, A. Talib, N. C. Ani, N. Ahmad, A. Muslihati, N. M. Rosni, A review of graphene materials-based sensors, *Current Advances in Microdevices and Nanotechnology (Series1)*, 2019, pp. 101–130.

43 N. M. Ndiaye, B. D. Ngom, N. F. Sylla, T. M. Masikhwa, M. J. Madito, D. Momodu, T. Ntsoane and N. Manyala, Three dimensional vanadium pentoxide/graphene foam composite as positive electrode for high performance asymmetric electrochemical supercapacitor, *J. Colloid Interface Sci.*, 2018, **532**, 395–406.

44 R. Saito, M. Hofmann, G. Dresselhaus, A. Jorio and M. Dresselhaus, Raman spectroscopy of graphene and carbon nanotubes, *Adv. Phys.*, 2011, **60**(3), 413–550.

45 M. Dresselhaus, A. Jorio, G. Dresselhaus, R. Saito, A. Souza Filho and M. Pimenta, Raman spectroscopy of nanoscale carbons and of an isolated carbon nanotube, *Mol. Cryst. Liq. Cryst.*, 2002, **387**(1), 21–29.

46 X. Yan, T. Suzuki, Y. Kitahama, H. Sato, T. Itoh and Y. Ozaki, A study on the interaction of single-walled carbon nanotubes (SWCNTs) and polystyrene (PS) at the interface in SWCNT-PS nanocomposites using tip-enhanced Raman spectroscopy, *Phys. Chem. Chem. Phys.*, 2013, **15**(47), 20618–20624.

47 J. Shin, J. Kwak, Y.-G. Lee, S. Kim, M. Choi, S. Bae, S.-H. Lee, Y. Park and K. Chon, Competitive adsorption of pharmaceuticals in lake water and wastewater effluent by pristine and NaOH-activated biochars from spent coffee wastes: contribution of hydrophobic and π–π interactions, *Environ. Pollut.*, 2021, **270**, 116244.

48 E. I. Unuabonah, M. O. Omorogie and N. A. Oladoja, Modeling in adsorption: fundamentals and applications, in *Composite Nanoadsorbents*, Elsevier, 2019, pp. 85–118.

49 A. O. Adeola, G. Kubheka, E. Chirwa and P. B. C. Forbes, Facile synthesis of graphene wool doped with oleylamine-capped silver nanoparticles (GW-αAgNPs) for water treatment applications, *Appl. Water Sci.*, 2021, **11**(11), 1–15.

50 S.-J. Zou, Y.-F. Chen, Y. Zhang, X.-F. Wang, N. You and H.-T. Fan, A hybrid sorbent of α-iron oxide/reduced graphene oxide: studies for adsorptive removal of tetracycline antibiotics, *J. Alloys Compd.*, 2021, **863**, 158475.

51 E. E. Jasper, V. O. Ajibola and J. C. Onwuka, Nonlinear regression analysis of the sorption of crystal violet and methylene blue from aqueous solutions onto an agro-waste derived activated carbon, *Appl. Water Sci.*, 2020, **10**(6), 1–11.

52 K. Nebaghe, Y. El Boundati, K. Ziat, A. Naji, L. Rghioui and M. Saidi, Comparison of linear and non-linear method for determination of optimum equilibrium isotherm for adsorption of copper (II) onto treated Martil sand, *Fluid Phase Equilib.*, 2016, **430**, 188–194.

53 A. O. Adeola, J. de Lange and P. B. C. Forbes, Adsorption of antiretroviral drugs, efavirenz and nevirapine from aqueous solution by graphene wool: Kinetic, equilibrium, thermodynamic and computational studies, *Appl. Surf. Sci.*, 2021, **6**, 100157.

54 E. T. Anthony, M. O. Ojemaye, A. I. Okoh and O. O. Okoh, Synthesis of CeO_2 as promising adsorbent for the management of free-DNA harboring antibiotic resistance genes from tap-water, *Chem. Eng. J.*, 2020, **401**, 125562.

55 A. O. Adeola and P. B. C. Forbes, Assessment of reusable graphene wool adsorbent for the simultaneous removal of selected 2–6 ringed polycyclic aromatic hydrocarbons from aqueous solution, *Environ. Technol.*, 2022, **43**(8), 1255–1268.

56 L. Fu, J. Li, G. Wang, Y. Luan and W. Dai, Adsorption behavior of organic pollutants on microplastics, *Ecotoxicol. Environ. Saf.*, 2021, **217**, 112207.

57 S. Lamichhane, K. B. Krishna and R. Sarukkalige, Polycyclic aromatic hydrocarbons (PAHs) removal by sorption: a review, *Chemosphere*, 2016, **148**, 336–353.

58 L. Jin, Y. Wang, F. Yan, J. Zhang and F. Zhong, The synthesis and application of nitrogen-doped graphene quantum dots on brilliant blue detection, *J. Nanomater.*, 2019, **2019**, 1–9.

59 C. Qu, D. Zhang, R. Yang, J. Hu and L. Qu, Nitrogen and sulfur co-doped graphene quantum dots for the highly sensitive and selective detection of mercury ion in living cells, *Spectrochim. Acta, Part A*, 2019, **206**, 588–596.

60 O. J. Achadu, I. Uddin and T. Nyokong, Fluorescence behavior of nanoconjugates of graphene quantum dots and zinc phthalocyanines, *J. Photochem. Photobiol., A*, 2016, **317**, 12–25.

61 E. T. Anthony, M. O. Alfred, T. D. Saliu and N. A. Oladoja, One-pot thermal synthesis of Ceria/Montmorillonite composite for the removal of hexavalent chromium from aqueous system, *Surf. Interfaces*, 2021, **22**, 100914.

62 I. A. Ololade, A. O. Adeola, N. A. Oladoja, O. O. Ololade, S. U. Nwaolisa, A. B. Alabi and I. V. Ogungbe, In situ modification of soil organic matter towards adsorption and desorption of phenol and its chlorinated derivatives, *J. Environ. Chem. Eng.*, 2018, **6**(2), 3485–3494.